



1 **A new accurate low-cost instrument for fast synchronized spatial measurements of light**  
2 **spectra**

3 Bert G. Heusinkveld, Wouter B. Mol, Chiel C. van Heerwaarden

4 *Meteorology and Air Quality Group, Wageningen University & Research, P.O. Box 47, 6700 AA*  
5 *Wageningen, the Netherlands*

6 **Abstract**

7 We developed a cost-effective Fast Response Optical Spectroscopy Time synchronized instrument  
8 (FROST). FROST can measure 18 light spectra in 18 wavebands ranging from 400 to 950 nm with a 20  
9 nm full width half maximum bandwidth. The FROST 10 Hz measurement frequency is time-synchronized  
10 by a Global Navigation Satellite System (GNSS) timing pulse and therefore multiple instruments can be  
11 deployed to measure spatial variation of solar radiation in perfect synchronization. We show that FROST  
12 is capable of measuring broadband shortwave, global horizontal, total irradiance (GHI) despite its limited  
13 spectral range.

14 It is very capable of measuring Photosynthetic Active Radiation (PAR) because 11 of its 18 wavebands  
15 are situated within the 400 to 700 nm range. A digital filter can be applied to these 11 wavebands to  
16 derive the Photosynthetic Photon Flux Density (PPFD) and retain information of the spectral composition  
17 of PAR radiation.

18 The 940 nm waveband can be used to derive information about atmospheric moisture.

19 We showed that the silicon sensor has undetectable zero offsets for solar irradiance settings and that the  
20 temperature dependency as tested in an oven between 15°C and 46°C appears very low ( $\sim 250$  ppm  $K^{-1}$ ).  
21 For solar irradiance applications, the main uncertainty is caused by our Poly Tetra Fluor Ethylene (PTFE)  
22 diffuser (Teflon), a common type of diffuser material for cosine-corrected spectral measurements. The  
23 oven experiments showed a significant jump in PTFE transmission of 2% around 21°C.

24 The FROST total cost ( $<€200$ ) is much lower than current field spectroradiometers, PAR sensors or  
25 Pyranometers, and includes a mounting tripod, solar power supply, datalogger and GNSS and waterproof  
26 housing. The FROST is a fully stand-alone measurement solution. They can be deployed anywhere with  
27 their own power supply and can be installed in vertical in-canopy profiles as well. This low cost makes it  
28 feasible to study spatial variation of solar irradiance using large grid high-density sensor set-ups or to  
29 use FROST to replace existing PAR sensor for detailed spectral information.

30 **1. Introduction**

31 Understanding solar irradiance and its interaction with clouds and vegetation is of utmost importance to  
32 unravel the complexity of feedback systems that determine our weather and climate. Cloud-shading  
33 dynamics of irradiance are highly dynamic (Lohmann, 2018) and Cloud-Resolving Models (CRM) are  
34 unable to resolve short time intervals and small spatial scales. At grid scales below 1 km, 3-D radiative  
35 transfer models can greatly improve the 3-D surface and atmosphere heating rates in atmospheric  
36 models (Calahan et al., 2005, Jakub & Mayer, 2015). A good example is the complexity of the radiative  
37 effects of shallow cumulus clouds and its interactions with a vegetated surface. Traditional 1-D radiation  
38 models produce unrealistic surface radiation fields but Menno et al. (2020) showed that a 3-D radiation  
39 transfer model could greatly improve the coupling mechanisms between clouds and the land surface. The  
40 small circulations, turbulence and combined cloud microphysics in convective boundary layers are both  
41 highly non-linear and complex. CRMs are crucial for improving weather forecasting models and for the  
42 energy meteorology sector. Kreuwel et al., 2020 showed that solar powered grid loading is highly  
43 dynamic and especially so for smaller household PV systems, leading to grid overloading challenges at  
44 very short time intervals of seconds. High quality observations both in high resolution spatially and with  
45 a high temporal resolution are required to test such models but so far such observations are lacking  
46 (Guichard and Couvreux, 2017).



47 Yordanov et al., 2013 showed that cloud enhancements can significantly increase solar irradiance levels  
48 (>1.5 times), which result in peak irradiance levels well exceeding extraterrestrial levels, even at high  
49 altitudes and latitudes (Yordanov, 2015). They used fast response silicon sensors and their highest  
50 detected irradiance bursts lasted about 1 s, which led them to believe that the required light sensor  
51 response time should be at least 0.15 s, much faster than traditional thermopile pyranometers with a  
52 response time of several seconds. The slow response time of those thermopile sensors is related to the  
53 thermal mass of the thermopile sensor. Semiconductor light sensors respond faster because photons  
54 directly mobilize electrons that can be measured directly. The downside of semiconductor light sensors is  
55 their limited and non-linear spectral response, and temperature sensitivity. Thermopile based  
56 pyranometers are also expensive as compared to a silicon-based solution, which limits their large-scale  
57 use in meteorological measurement networks. Martinez et al., 2009, showed that a factor 10 reduction in  
58 pyranometer costs as compared to a thermopile sensor is possible with the use of a silicon photodiode,  
59 however their spectral response is limited (their version: 400 to 750 nm) and it has a nonlinear spectral  
60 response. A major solar spectral change occurs in the infrared due to water absorptions bands, which  
61 leads to an overestimation for clear sky conditions and an underestimation for overcast skies when  
62 calibrated for average weather conditions.

63 The spectral response limitations of the photodiode used by Martinez et al., 2009, can be improved with  
64 a wider spectral response silicon type pyranometer such as applied in the LI-COR 200-SZ as  
65 demonstrated by Michalsky et al., 1990. They compared the LI-COR 200-SZ with a thermopile  
66 pyranometer (Kipp & Zonen CM-11). The CM-11 has a flat spectral response (300 to 2500 nm) whereas  
67 the LI-COR 200-SZ exhibits a very nonlinear and limited spectral response starting at 400 nm and  
68 increasing 5-fold in sensitivity towards its peak around 1000 nm, then sharply dropping off to zero at  
69 1100 nm. Their main uncertainty related to the temperature dependance of silicon sensors. After a  
70 temperature correction, they performed similar to thermopile pyranometers (11.4 W m<sup>-2</sup> rms errors)  
71 under clear and cloudy sky conditions. This is surprisingly accurate because LI-COR calibrates their  
72 pyranometer against a reference thermopile pyranometer and therefore a change in solar spectrum may  
73 affects its accuracy. Michalsky et al., 1990, argued that the clear or cloudy sky GHI spectra is similar  
74 because of clouds mixing the direct and blue skylight. This, however, is contradicted by a recent study by  
75 Durand et al., 2021, where they investigated the spectral differences between clear and overcast skies.  
76 They showed that clouds, in relative terms, enrich GHI spectra in wavelengths < 465 nm and depleted in  
77 wavelengths > 465 nm. This may well explain why the LI-COR sensor performed so well because its  
78 main sensitivity is in wavelengths > 465 nm thus indirectly correcting for the reduced infrared in the  
79 major water absorption bands beyond its spectral range.

80 Optoelectronics are evolving rapidly and innovations in semiconductor integration with optical  
81 components and microprocessors are paving the way for cost-effective spectrometers that can provide  
82 even temperature compensated spectral details about solar radiation. A leading manufacturer in this field  
83 is AMS (Austria Micro Systems, Austria) and offers various intelligent light sensing products that are  
84 capable of measuring light intensity within multiple optical wavebands. These sensors are mass-  
85 produced, resulting in low-cost sensors. Tran and Fukuzawa, 2020, tested such a cost effective 18 band  
86 multispectral sensor (AS7265x, AMS) for spectroscopy of fruit (between 400 and 950 nm) and useful  
87 information could be derived. Such spectroscopy sensors would be very interesting for solar irradiance  
88 measurements. The spectral signature of radiation is very relevant to quantify since clouds and air  
89 pollution modify the solar light spectrum and light scattering. Additionally, multiple reflections between  
90 various ground and water surfaces and clouds will further influence the light spectral composition. This is  
91 especially relevant in the photosynthetic active radiation wavelengths (PAR) for vegetation cloud  
92 feedbacks since it affects photosynthesis and evapotranspiration (Durand et al., 2021).

93 The correct synchronization of the sensor grid measurements is essential and several options were  
94 considered such as a network configuration with synchronized triggering at fixed time intervals. Wires in  
95 the field were not an option due to logistic challenges, and radio communication could be possible but  
96 adds to the cost with reduced reliability due to radio interference. As a robust option, a GNSS receiver  
97 was considered that constantly synchronizes its internal time to an international clock standard. Similar



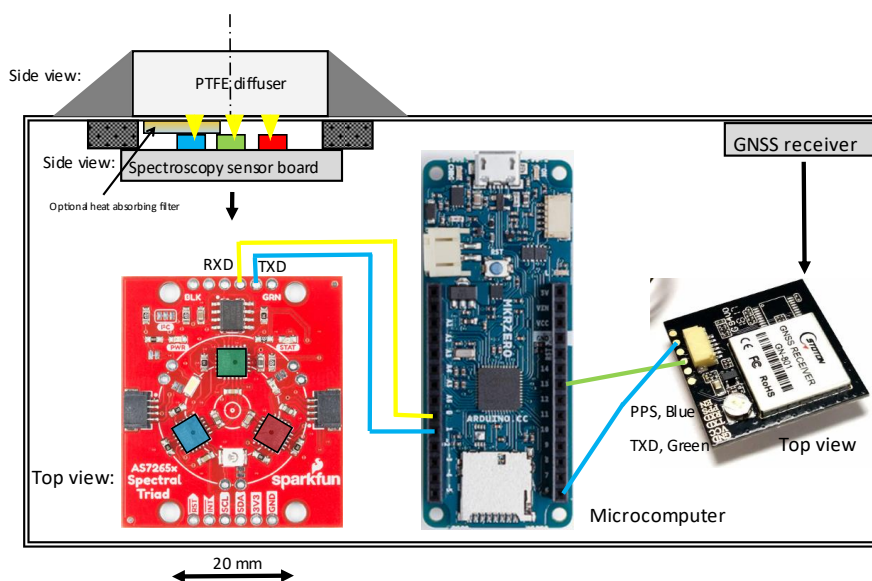
98 timing synchronizations are used for sensors grids in seismic activity monitoring of volcanos where  
 99 timing is essential to determine seismic propagation and where synchronization accuracy of 50 ns could  
 100 be achieved (Lopez Peirera et al., 2014).

101 Here we present the development of a cost-effective fast-response solar light sensor grid for spatially  
 102 and temporally high resolution multiple light waveband resolved GHI measurements. The required large  
 103 number of sensors requires cost effective design optimization.

104 Additionally, we tested these sensors for meteorological, photosynthesis and remote sensing applications  
 105 and tested performance both in the lab and in field experiments.

## 106 2. Instrument design and measurement method

107 The measurement system we developed is depicted in Figure 1 and consists of a silicon light sensor  
 108 chipset (AMS AS7265x), a GNSS for time synchronization, a cosine corrector light diffusing input port,  
 109 and a microcomputer. See Table 1 for a list of components.



110

111 Figure 1: Mechanical layout and wiring diagram of the FROST spectrometer (Sensor: 3.2 mm below a  
 112 Teflon filter with radius of 32 mm). For easy identification we color-coded the three light sensors (blue,  
 113 green and red), each measuring 6 channels.

114 Time-synchronized measurements are achieved using a hardware GNSS receiver timing pulse (PPS) to  
 115 trigger each measurement and time-stamped data is processed and collected by a microcomputer board  
 116 (Figure 1, Table 1).

117 Table 1: List of components for the waterproof solar powered spectrometer.

Component	Manufacturer and model	Price (€)
Spectroscopy chipset	AS7265x spectral sensors triple AMS (Austria) with interfacing logic mounted on a PCB by Sparkfun (U.S.A.)	70
Optical filter	Schott heat-absorbing colored glass filter KG3 or KG1, 2 mm (Germany)	11
UV-sensor	GUVA-S12SD	1.70
PTFE diffuser	32 mm diameter, cut from a plate (S-Polytec GmbH, Germany)	3



<b>GNSS receiver</b>	<b>TOPGNSS GN-901, China, GPS and Glonass receiver</b>	<b>6</b>
<b>Microcomputer</b>	<b>Arduino MKR Zero</b>	<b>23</b>
<b>Memory card</b>	<b>Kingston Canvas Select Plus microSDHC 32GB</b>	<b>4</b>
<b>Breadboard</b>	<b>Solderless PCB breadboard Mini protoboard</b>	<b>0.90</b>
<b>Solar panel</b>	<b>First Solar, China, CNC165x165-5, Polycrystalline, 4.2 W, 5 V, 840 mA, 165x165 mm</b>	<b>7</b>
<b>Battery</b>	<b>Li-Ion battery LP906090JH, Jauch, Germany</b>	<b>30</b>
<b>Charger controller</b>	<b>Mini Solar Lipo Charger board CN3065</b>	<b>1.40</b>
<b>Box</b>	<b>Outdoor Junction Box 100x150x70mm waterproof IP65, Shockproof ABS plastic. ManHua, China (AliExpress)</b>	<b>9</b>
<b>Tripod mount adapter</b>	<b>Camera metal shoe mount adapter 1/4" thread</b>	<b>0.75</b>
<b>Tripod</b>	<b>König KN-TRIPOD21/4 camera tripod pan &amp; tilt 130 cm</b>	<b>12</b>
<b>Ground anker</b>	<b>Tent herring</b>	<b>1</b>
<b>Silicone adhesive sealant</b>	<b>Permatex 81158 or Bizon Black Silicone Adhesive</b>	<b>1</b>

118

119 The light sensors are mounted on camera tripods, which makes leveling easy (Figure 2). A camera metal  
 120 shoe mount adapter was glued under the polycarbonate housing for fast mounting. For winds >6 m/s it  
 121 is advised to use tent herrings to fix the tripod to the ground. The power consumption is 0.5 W and a 6  
 122 Ah LiPo battery together with a LiPo charge regulator is a reliable power supply solution for the Dutch  
 123 climate from April - September. The 4.2 W polycrystalline solar panel is glued on a special shaped  
 124 wooden frame that slides over the tripod center tube, with the solar panel sides resting against the two  
 125 outer tripod legs. It is fixed to the rear leg with a thin metal wire. Hot glue appeared unsuitable for the  
 126 panels and it is advised to use epoxy glue.

127 The PTFE diffuser was glued to the box by roughening the surfaces and using a black silicone adhesive  
 128 around the diffuser edges.



129

130 Figure 2: FROST with solar panel mounted on a camera tripod.

### 131 2.1 Light sensor



132 The light sensing element is the AMS AS7265x, a smart spectrometer sensor capable of measuring light  
133 at 18-Channel 20 nm full width half maximum (FWHM) bandwidth from visible and near infrared spectral  
134 bands (410 to 940 nm) with an electronic shutter (manufacturer: AMS, Australia). The spectrometer  
135 consists of three separate integrated circuits with each including six silicon-based photo diodes with  
136 integrated optical bandpass interference filters, micro-lenses, a programmable analog amplifier, and an  
137 analog to digital converter and a microprocessor. We will identify the AS72651, -52, -53 as the blue, red  
138 and green sensor and indicated in Figure 1. The integrated light interference filters are directly deposited  
139 on the silicon. Factory calibration values are stored inside the internal memory. Two serial  
140 communication options are available for interfacing with a microcomputer; a Universal Asynchronous  
141 Transmission (UART) and a synchronous serial transmission (I2C) port. The three light sensor view  
142 angles are limited by the chip housing light input port to 41°, which ensures that the optical interference  
143 band filters stay within the +/-10 nm FWHM specifications. AMS states that their filter stability (in time  
144 and against temperature) is not detectable but does not provide further specifications. They do mention  
145 that the wavelength accuracy is within +/- 10 nm. The AS7265x triple set of light sensor chips, each  
146 capturing six light wavebands, poses a challenge to couple optically all three to the same sensing area  
147 and to assure a good cosine response needed for the accurate measurement of GHI. The limited opening  
148 angle poses an additional challenge for GHI measurements since they require a viewing angle of 180°,  
149 therefore an achromatic cosine-corrected diffuser is required.

## 150 **2.1 Diffuser material**

151 Teflon (PTFE) material is commonly used as an effective light diffuser, with a large spectral transmission  
152 range starting below 300 nm, and is available from various producers. However, PTFE light transmittance  
153 exhibits a temperature dependency caused by a major phase change in its crystalline structure at 19°C.  
154 The phase change can cause a significant change in transmittance. Yliantilla and Schreden, 2004, tested  
155 three commercially available PTFE diffusers and found transmission changes between 1 and 4%. By  
156 comparison, they also showed a quartz diffuser with a linear response to temperature (0.035% °C<sup>-1</sup>)  
157 without jump. Despite this, PTFE was nevertheless chosen as a cost-effective diffuser to maximize the  
158 spatial number of sensors. The diffusers were cut from PTFE plates (S-Polytec GmbH, Goch, Germany)  
159 using a vice and a hole punch to press round diffusers. A 10.6 and 2.0 mm thick diffuser were tested.  
160 The transmission temperature dependency of our PTFE diffusers was tested in a temperature-controlled  
161 oven with cooler (WTS Binder, Germany with a EURO THERM temperature controller). The oven is  
162 equipped with a front glass door and the lowest possible temperature setting was kept above the  
163 dewpoint temperature of the laboratory to avoid moisture condensation issues. An LED light source (LCS,  
164 17 W, 2500 Lumen) was chosen for its high output and limited thermal infrared, and powered by a  
165 stabilized voltage power supply. The LED was placed outside the oven in front of the oven's glass door  
166 about 1 m away to minimize lamp heating. A second light sensor was placed outside the oven next to the  
167 lamp to monitor its output. Diffuser light transmission measurements were corrected for variation in  
168 lamp output. Subsequently the light sensor without a diffuser was tested.

169 The spectrometer performance was also tested at the DWD (German Weather Service) radiation  
170 calibration facility in Lindenberg, Germany. The spectrometer output was compared against a calibrated  
171 xenon light source and the intensity was adjusted by varying the lamp sensor distance between 0.5 m  
172 and 0.7 m. The possible spectral crosstalk of infrared light was tested by placing a very steep long pass  
173 interference filter with a Cut-On Wavelength of 1000 +/-9 nm (Dielectric Coated Long pass Filter, 25.4  
174 mm diameter, 1.1 mm thick, transmission >95%, OD5 Blocking, Edmund optics, Stock #15-463) in front  
175 of the sensor. The long pass filter blocks all sensor wavebands and any remaining signal is then  
176 considered infrared crosstalk. The position of the optical waveband filters was tested using a Cary  
177 (Agilent, USA) UV-Vis NIR spectrophotometer at Wageningen University, The Netherlands.

## 178 **2.2 Cosine response**

179 The cosine response was determined by placing a LED light source (LED light bulb 2500 Lumen, diameter  
180 0.1 m) and our light sensor five m apart, both on tripods at 1 m height. Since a darkroom was not  
181 available, the measurements were performed outdoors at night to avoid reflection from ceilings and



182 walls. A night with low humidity was chosen to minimize aerosol light scattering. The direction of the  
183 light sensor was adjusted from 0° (viewing the light source) to 90° (perpendicular to the light beam). To  
184 keep the distance between the sensor and light source constant during rotation, the plane of rotation was  
185 exactly located at the diffuser surface. A shading screen was placed between the light source and sensor  
186 to shade the ground surface to avoid any light reflection into the sensor.

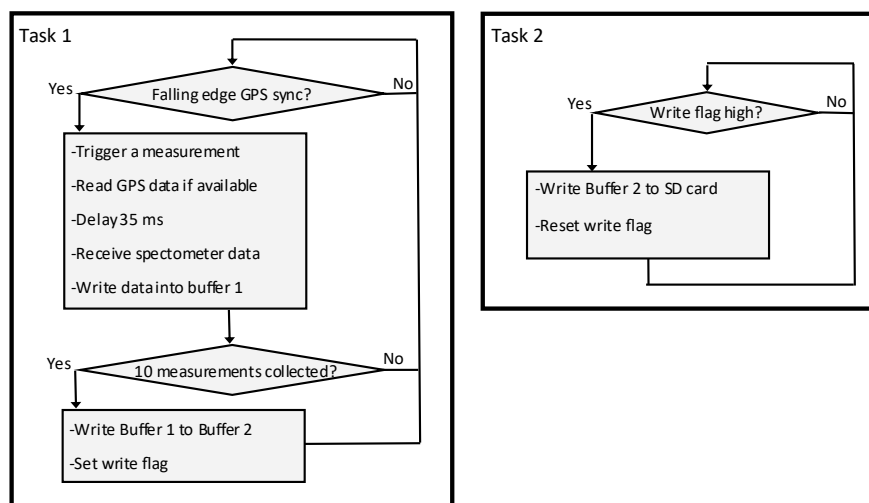
#### 187 **2.4 Time synchronization**

188 Instead of using a GNSS for synchronizing an internal clock or using the serial date and time output, we  
189 use the very precise (<100 ns accuracy) hardware timing pulse of a GNSS module to trigger each  
190 measurement directly (at 10 Hz.). The data is time-stamped with the GNSS date and time output. A  
191 special GNSS receiver was selected that also outputs a programmable timing pulse for synchronization  
192 purposes (better than 50 ns). As a bonus, it also provides location data within a few meters. These  
193 receivers can be purchased for less than 6€ (Table 1).

#### 194 **2.5 Datalogging**

195 The datalogging of the GNSS date, time, latitude, longitude and the 18 channel spectroscopy  
196 measurements at 10 Hz results in a dataflow of >100 MB data per day. The spectroscopy sensor outputs  
197 ASCII data and the bandwidth of the I2C interface on the spectroscopy side were insufficient, thus the  
198 UART serial interface was selected. The sensor can be triggered by serial command to do a measurement  
199 and this command in turn is triggered by the hardware timing pulse of the GNSS.

200 For datalogging, the MKR Zero of the Arduino family microprocessor platforms was chosen. It is a cost-  
201 effective and low power datalogging solution using a 48 MHz SAMD21 Cortex 32bit low power ARM MCU  
202 and a built in micro SD card holder (max. 32GB). The challenge with this datalogging solution is that the  
203 default operating system cannot handle sustained data writing to an SD card at 10 Hz using linear  
204 programming. In fact, the SD card would regularly delay the measurements with an estimated 200 ms  
205 resulting in a loss of data (tested with a new, fast SD card with 85 MB/s max write speed). It therefore  
206 needs a microcontroller multitasking real-time operating system and thus FreeRTOS (freertos.org) was  
207 chosen to overcome this. Two tasks that run semi-parallel on the single core CPU were defined. The first  
208 task with the highest priority will initiate a measurement cycle at the falling edge of the hardware timing  
209 signal of the GNSS. Task 2 will trigger each second and writes the 10 Hz buffered data to the SD card  
210 (Figure 3).



211



212 Figure 3: Multitasking software implementation for synchronized measurements and data storage. Each  
213 Buffer can contain 10 rows of data. The program is available at zenodo.org (DOI  
214 10.5281/zenodo.6945812).

215 *Restricted access for review:*

216 [https://zenodo.org/record/6945812?token=eyJhbGciOiJIUzUxMiIsImV4cCI6MTY3MjQzNzU5OSwiaWF0IjozNjU5MzQ0NTQzfQ.eyJkYXRhIjpb7InJlY2lkIjo2OTQ1ODEyfSwiaWQiOiI1MDE5LCJybmcQiOiJmMzc3ZTA4OCJ9.QO9Yid2igwh3pHwQFzcw\\_LuwTnkGsGYGjiALRqByop6JcyAAJBjy5D9zKHIGv0cIYZEspWaguAcmcAK6RFP CqQ](https://zenodo.org/record/6945812?token=eyJhbGciOiJIUzUxMiIsImV4cCI6MTY3MjQzNzU5OSwiaWF0IjozNjU5MzQ0NTQzfQ.eyJkYXRhIjpb7InJlY2lkIjo2OTQ1ODEyfSwiaWQiOiI1MDE5LCJybmcQiOiJmMzc3ZTA4OCJ9.QO9Yid2igwh3pHwQFzcw_LuwTnkGsGYGjiALRqByop6JcyAAJBjy5D9zKHIGv0cIYZEspWaguAcmcAK6RFP CqQ)

## 220 **2.6 Field experiments**

221 The field experiments were conducted at various locations. At the Veenkampen weather station,  
222 Wageningen, The Netherlands (Lat.: 51.981°, Long.: 5.620°). Sensor performance was tested against  
223 GHI measurements and a spectrophotometer. Although GHI ( $Q_{gI}$ ) is directly measured with a  
224 pyranometer, it was decided to use the pyrliometer and diffuse radiation sum to reduce cosine  
225 response errors. The instruments consist of a Kipp&Zonen Pyrliometer CMP1 with a calibration  
226 accuracy of +/-0.5% and a first class pyranometer CM21 for diffuse radiation measurements with a time  
227 constant of 5 s, directional error < +/-10W m<sup>2</sup>, tilt error: +/- 0.2%, zero-offset due to T change: <2 W  
228 m<sup>2</sup> at 5K h-1, cosine response error: max +/-2% at 60°, max. +/-6% at 80°. Both instruments were  
229 mounted on a suntracker (EKO instruments with shading disk, Japan). On selected days the solar  
230 spectrum was measured with the ASD FieldSpec (U.S.A.) field spectroradiometer with a cosine collector,  
231 with a calibration made in 2021.

232 Additionally a large set of sensors were deployed during the FESSTVal campaign (<https://fesstval.de/>) at  
233 the German Weather Service (DWD) in Falkenberg, Germany, to study the spatial variation of solar  
234 irradiance (June 2021). For that campaign, it was crucial to obtain fast and time synchronized spatial  
235 solar irradiance measurements. Their Baseline Surface Radiation Network (BSRN) location at Lindenberg  
236 was used to test long-term stability from 22 June-31 August 2021.

237 The FROST was also deployed in a field experiment in La Cendrosa, Spain (Lat: 41.692537, Long:  
238 0.931540) (from 14-22 July 2021. It was used, among other things, to study crop growth).

## 239 **3. Performance and applications**

240 The performance of the sensor, the temperature dependency of the diffuser and the time synchronization  
241 is presented below. Three versions of FROST are presented: one with a 10.6 mm diffuser, one with a 2  
242 mm diffuser including a correction filter on the blue sensor, and one with a 2 mm diffuser with two  
243 correction filters (on the blue and red sensor).

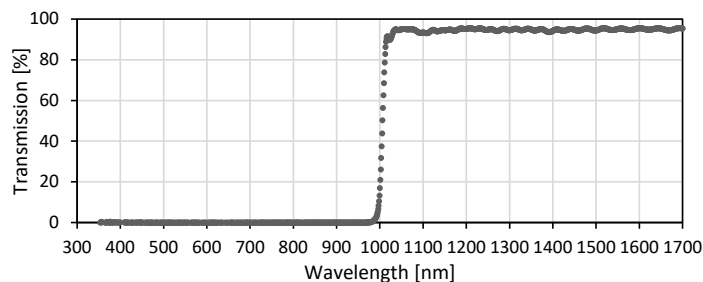
### 244 **3.1 Spectral response and temperature sensitivity**

245 According to the manufacturer specifications, the normalized (at peak wavelength) responsivity of their  
246 spectroradiometer has a good narrow band response (20 nm full width half maximum (FWHM)) and  
247 limited overlap for the 18 channels. Wavelength accuracy is within +/- 10 nm and this was confirmed by  
248 testing the sensor inside a Cary spectrophotometer. Unfortunately the Cary spectrophotometer had a  
249 limited spectral range so we could not test the crosstalk in the near infrared. Comparison of the  
250 spectroradiometer against a reference thermopile pyranometer CM21 (Kipp and Zoonen, The  
251 Netherlands) and a stabilized halogen light source. The intensity was adjusted by changing the lamp  
252 distance. The FROST non-linearity was a t least as good as the CM21 which has a non-linearity of < +/-  
253 0.2%. The factory-calibrated accuracy is 15% according to the manufacturer specifications. After initial  
254 testing using solar radiation as a light source for reflectance measurements of lawn grass, we were  
255 confronted with unusual data. The PAR region clearly showed very high reflection values, more than 5  
256 times of what is typical for such a surface.



257 We tested the sensor at the DWD radiation calibration facility in Lindenberg using a calibrated light  
258 source and an optical Long Pass interference (LP) filter that blocks all light below 1 micrometer. The  
259 blocking filter characteristics were tested in a Cary photo spectrophotometer (Figure 4).

260

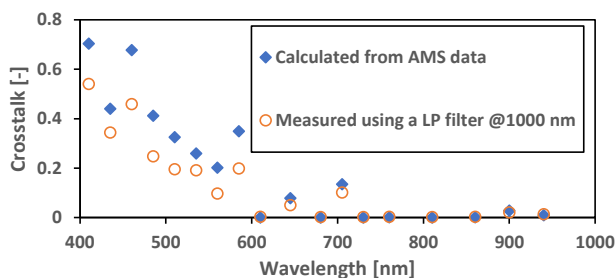


261

262 Figure 4: Transmission of the optical LP filter measured with a Cary photo spectrophotometer at the  
263 DWD, Lindenberg.

264

265



266

267 Figure 5: Measured spectroscopy sensor infrared crosstalk from wavelengths >1000 nm, tested with a  
268 Xenon lamp and an optical long pass filter (LP at 1000 nm) and calculated from spectral response data as  
269 supplied by the manufacturer (AMS).

270 Figure 5 shows the fraction of infrared light (>1000 nm) within the sensor output for each of the 18  
271 channels. The sensor output was corrected for the LP filter transmission loss (about 5%, see Figure 4).  
272 Note that the crosstalk is larger than during solar radiation measurements because a Xenon light source  
273 contains a large amount of infrared radiation. Cloudy conditions would further reduce crosstalk. For clear  
274 sky conditions, the crosstalk would be about half of the Xenon light. The blue dots show the calculated  
275 crosstalk using the AMS sensor spectral filter response data obtained through personal communication  
276 with the manufacturer. The measured crosstalk on the blue sensor appears to be slightly better. The  
277 crosstalk is very large in the visible light range and confirms the provided filter transmission curves from  
278 AMS (personal communication). Note that those transmission curves are not available on the publicly  
279 available datasheet. Figure 5 shows that only half of the channels provide the correct spectral  
280 information (if calibrated correctly using the data from Figure 6). However, there are enough channels to  
281 measure the so-called red edge around 700 nm in vegetation light transmission and reflection. This  
282 opens up applications for vegetation growth measurements without further modifications.

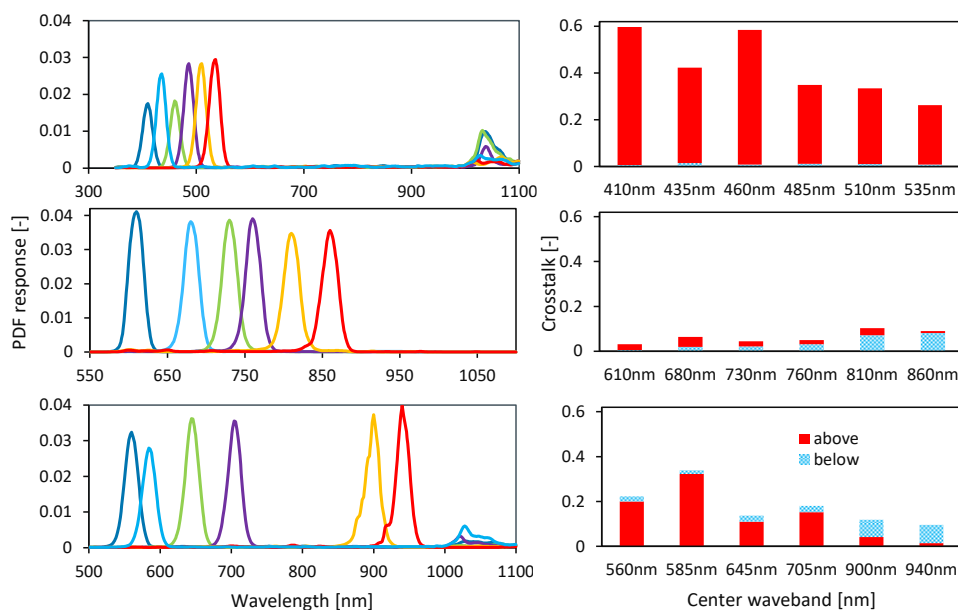
283 All channels in the blue sensor and some of the channels (650 and 685 nm) in the red sensor have very  
284 high crosstalk from the 1000 to 1100 nm range, but the crosstalk makes the sensor cover a larger range  
285 of the solar spectrum. It is therefore still usable if this can be quantified.

286 After consultation with the manufacturer, they clarified that the AS72653 sensor has a strong crosstalk in  
287 the near infrared. The sensor was meant to be used with LED light for spectral reflectance measurement





288 applications. They recommend for each sensor a specific LED, and therefore each reflectance  
289 measurement would consist of 3 separate measurements with each using one sensor and with one  
290 specific LED at a time.

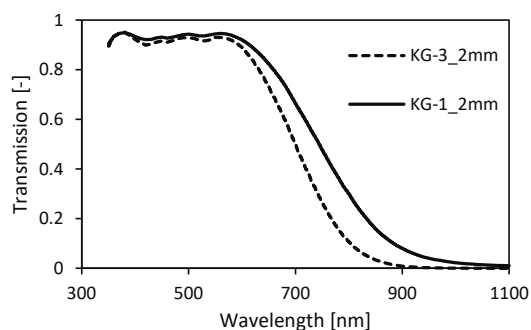


291

292 Figure 6: Spectral response of the 3 sensors, Probability Density Functions (PDF) calculated from data  
293 provided by manufacturer AMS (personal communication). The crosstalk fraction of sensor response at  
294 30 nm above and 30 nm below the center wavelength of each band is depicted (sensor only).

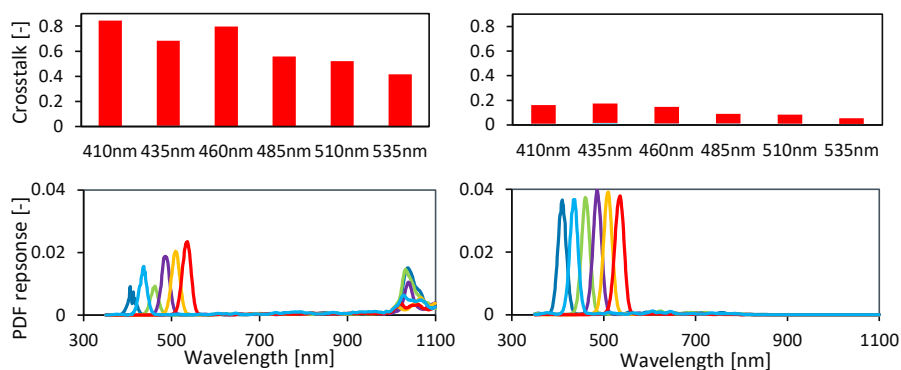
295 Figure 6, right panels, shows that the crosstalk, defined as the signal above or below 3x 0.5 FWHM from  
296 the center wavelength, is large (up to 60%) in the PAR range for the blue sensor and mainly from the  
297 infrared beyond 1 micrometer. The green sensor performs much better and does not exhibit infrared  
298 crosstalk. The red sensor has an issue mainly on the first two channels.

299 To remove infrared crosstalk, an optical short pass filter is required. However, a filter with a sharp cut-off  
300 at 1000 nm is, to our knowledge, not available or probably very expensive and sensitive to angle of  
301 incidence. Cost-effective short pass filters are made from heat-absorbing glass and has a dye added to  
302 the glass that absorbs infrared radiation. However, these heat-absorbing filters do not have a steep filter  
303 response and therefore ineffective to correct the red sensor without attenuating the 900 and 940 nm  
304 channels too much. The Schott heat-absorbing filters KG3 and KG1 appear to offer a good solution for  
305 the blue sensor (Figure 7). The remaining crosstalk is mainly related to the slightly broader filter  
306 response. The first 4 channels of the red sensor (Figure 8) can also be improved. However, such a  
307 correction filter for the red sensor would increase crosstalk from shorter wavelengths for the 900 and  
308 940 nm wavebands (see lower right panel in Figure 6) and greatly reduce signal strength. For accurate  
309 PAR measurements, and when the 900 and 940 nm channel are not needed, it is recommended to use  
310 the less strong KG-1 filter for the red sensor.



311

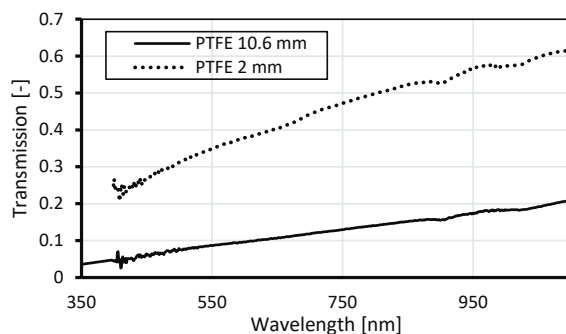
312 Figure 7: Correction filters for the infrared crosstalk: Schott heat-absorbing filters (adapted from Schott  
313 AG manufacturer data).



314

315 Figure 8: Spectral response and crosstalk of the blue sensor, left panels: 10.6 mm diffuser, right panels:  
316 2 mm diffuser including a heat absorbing filter (Schott KG-3), calculated from manufacturer data.

317 Because of the limited view angle of the spectroscopy sensors (40°) it is crucial to add a light diffuser.  
318 The PTFE light diffuser transmission is shown in Figure 9 (measured with the ASD FieldSpec). Note that it  
319 enhances infrared crosstalk.

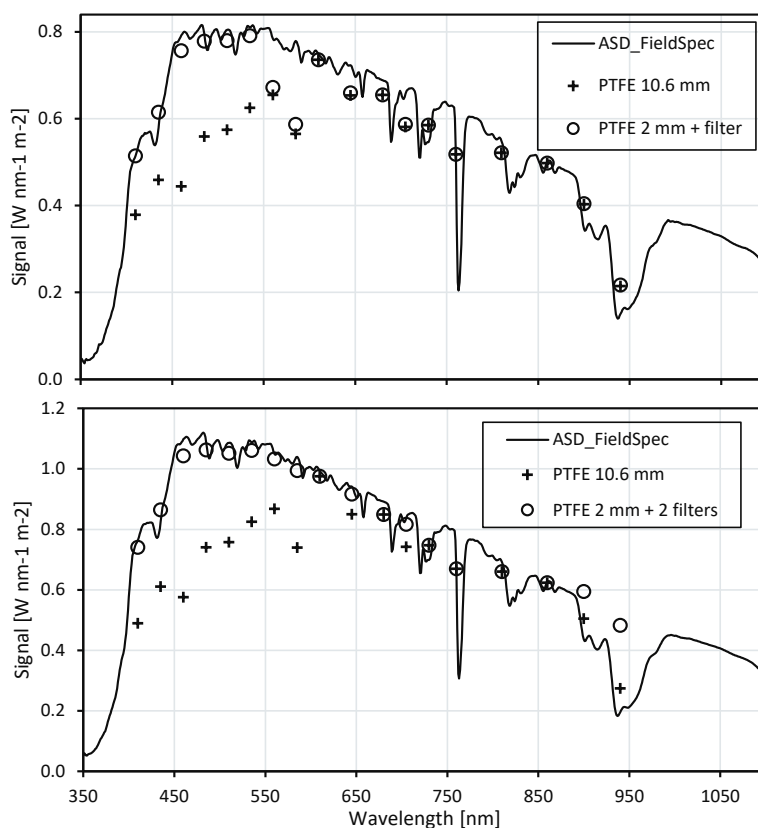


320

321 Figure 9: Transmission of PTFE diffusers measured with an ASD FieldSpec spectroradiometer.



322 The reduced transmittance in the shorter wavelengths enhances the near infrared crosstalk. The  
323 combined effect of sensor and PTFE spectral response with or without correction filters is shown in Figure  
324 10. Three versions of the spectrophotometer were developed, one with a 10 mm diffuser to improve  
325 cosine response, a second version with a 2 mm diffuser and a correction filter on the blue sensor, and a  
326 third version with 2 mm diffuser and correction filters on the blue and red sensor. The spectral selective  
327 quality on real world measurements (Figure 10) was calculated from the combined effect of the  
328 spectrophotometer filter characteristics (Figure 6), diffuser (Figure 9) and Schott correction filters (Figure  
329 7).



330

331 Figure 10: Outdoor measurements during clear sky conditions, Wageningen, lower panel: 15 May 2022,  
332 14:24 h UTC, upper panel: 11 March 2022, 13:35 h UTC.

333 Figure 10 shows that the first 6 channels, if uncorrected with a heat absorbing filter underestimate the  
334 irradiance levels at the expected wavebands because these bands are very sensitive to the infrared  
335 region between 1000 and 1100 nm. The heat-absorbing filters effectively remove this crosstalk. It also  
336 shows that the red sensor should not be equipped with such a filter if the 900 and 940 nm wavebands  
337 are important, for example to estimate column atmospheric moisture (see application section, Figure  
338 14).

339 The procedure to calibrate each waveband of FROST would require an accurate spectrophotometer and a  
340 clear day. First, each of the 18 PDF band responses of the sensor (with or without a correction filter!)  
341 and diffuser combination is multiplied with the known solar spectra for a very clear day or measured with  
342 a calibrated spectrophotometer. This gives the  $nW m^{-2}$  reference value the FROST sensor should produce



343 for each waveband. Subsequently the FROST raw 18 wavebands outputs are multiplied by the AMS  
 344 calibration factors (since we use the uncalibrated output for fast measurement) and divided by the  
 345 reference values. The AMS spectroscopy sensor calibration values are written to the SD card at the very  
 346 start of the measurements.

347 The sensor output sensitivity is then expressed as counts per nW m<sup>-2</sup>. The normalized sensor response is  
 348 provided in Figure 6 and 8 and as Table s1 in supplementary materials. An example of sensitivity values  
 349 is presented in Table 2. These values were derived on 11 March 2022 13:35 UTC for the 10.6 mm  
 350 diffuser version and the 2 mm diffuser + 1 filter version. The 2 mm diffuser with 2 correction filters was  
 351 measured on 15 May 2022 (Figure 10). Note that these values are only valid for an integration value of  
 352 14 ms and a gain of 16. We not to use channels with Flag 2 or 3.

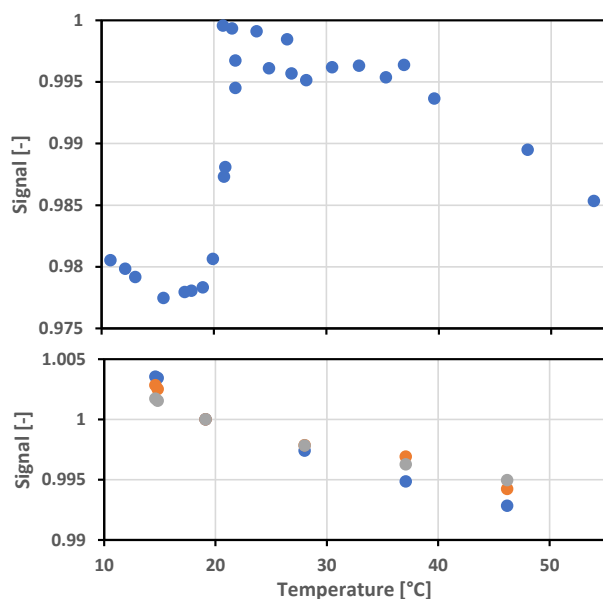
353 Table 2: Sensitivity of FROST with different configurations. The flags denote quality of measurement  
 354 (waveband accuracy). Flag 0: low crosstalk, Flag 1: crosstalk<20%, Flag 2: 20%<crosstalk<35%, Flag  
 355 3: crosstalk>40%.

Waveband [nm]	10.6 mm diffuser Sensitivity		2 mm diffuser+1 filter Sensitivity		2 mm diffuser+2 filters Sensitivity	
	[Counts nW-1]	Flag	[Counts nW-1]	Flag	[Counts nW-1]	Flag
610	116	0	474	0	494	0
680	132	0	503	0	436	0
730	156	0	549	0	554	0
760	156	0	413	0	387	0
810	188	0	673	0	651	0
860	194	0	760	0	649	0
560	51	2	253	2	186	0
585	70	2	333	2	195	0
645	55	1	256	1	168	0
705	70	1	295	1	117	0
900	90	0	348	0	19	3
940	107	0	395	0	25	3
410	94	3	153	0	157	0
435	100	3	200	0	206	0
460	144	3	211	0	218	0
485	96	3	209	0	217	0
510	94	3	213	0	221	0
535	84	3	204	0	213	0

356

### 357 3.2 Temperature sensitivity and drift

358 The diffuser and sensor were both tested for temperature effects. The measurements were corrected for  
 359 sensor temperature drift or drift in lamp output by measuring the lamp output with an extra sensor  
 360 outside the oven. The oven has an internal fan to assure a homogeneous temperature within the oven  
 361 chamber. The PTFE filter shows a significant jump in transmission around 21°C, then reaching a plateau  
 362 and slowly declining past 35°C (Figure 12, upper panel). The temperature was slowly increased and  
 363 stabilized for 30 minutes at each measurement point to minimize thermal delays in the PTFE material.



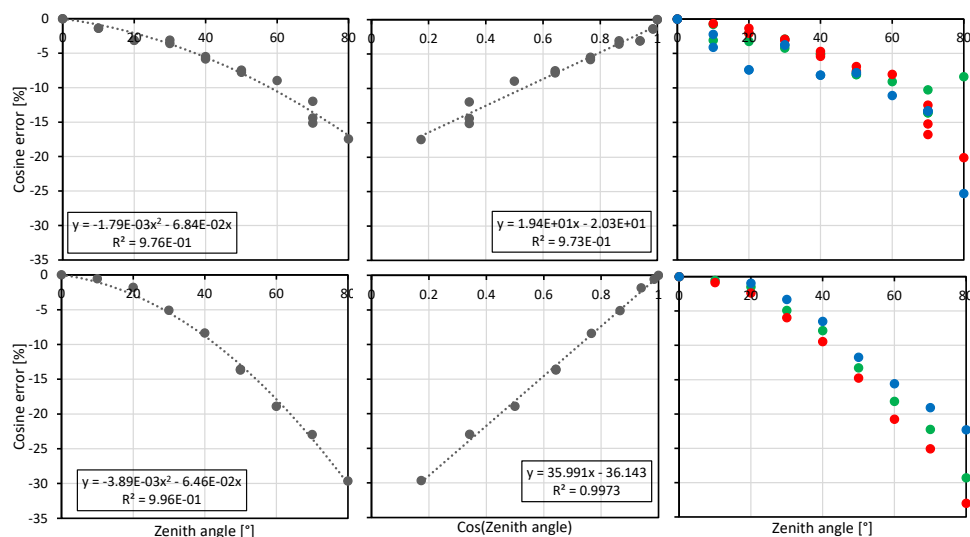
364

365 Figure 11: Temperature response; upper panel PTFE diffuser, lower panel 3 random light sensors (-250  
366 ppm).

367 Three spectroscopy sensor chipsets (3x 18 waveband) were oven tested for temperature sensitivity  
368 between 16 to 46°C. Overall temperature sensitivity is  $-250 \text{ ppm K}^{-1}$  with a small variation among the  
369 three sensors. Lower temperatures were not possible due to condensation issues when reaching the  
370 dewpoint temperature of the laboratory (Figure 11).

### 371 3.3 Cosine response and GHI

372 The cosine response measurements (outside, LED lamp) had a better performance for the 10 mm  
373 diffuser but nevertheless had some inconsistencies among the three sensors. We tried to improve the  
374 cosine response by leaving part of the sides uncovered but this caused a very high asymmetry among  
375 the three sensors. The explanation is that the three sensors do not have the same viewing angle location  
376 under the diffuser, thus some will see more from the side than other sensors. The side sensitivity is  
377 greatly reduced with a thinner filter but at the expense of a reduced cosine response (Figure 12).

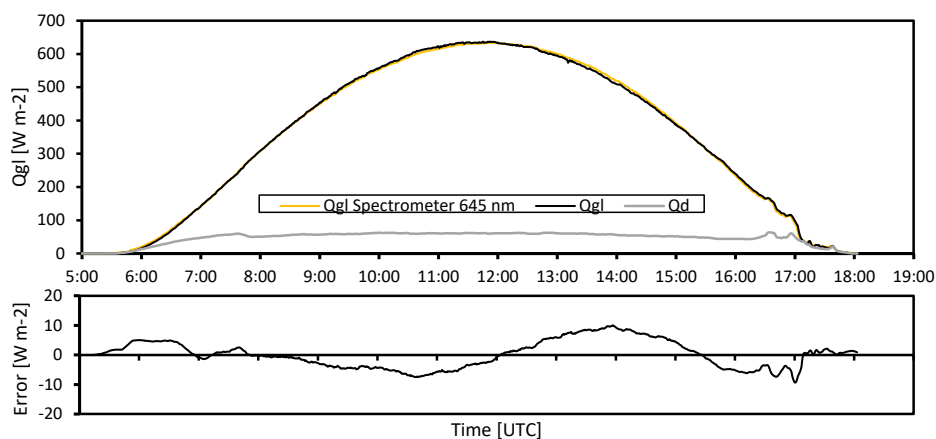


378

379 Figure 12: Upper panels: 10.6 mm diffuser (black sides), lower panel: 2 mm diffuser (sides painted  
380 black). The right panels are color-coded and represent the color code for each sensor integrated circuit.

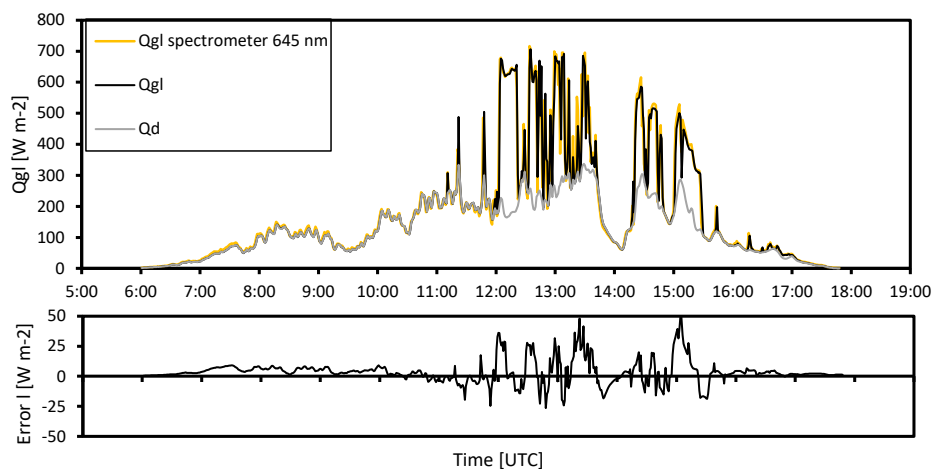
381 We found that most of the cosine response errors can be corrected afterwards and is demonstrated for  
382 the 2 mm filter, which had the largest cosine response error. The accurate measurement of GHI can be  
383 achieved by first correcting for the zenith angle response (see Figure 13, middle lower panel) and  
384 subsequently applying a second order linear regression against a reference pyranometer on one clear  
385 day (19 March 2021). Additionally, a correction for the limited spectral response is needed. We tested  
386 this calibration method for the average signal of all 18 wavebands and on single wavebands. The dataset  
387 contains clear sky days (Figure 13), overcast days (Figure 14) and rainy weather (Figure 15). The best  
388 overall results were achieved with either channel 645 or channel 705 nm, with residual errors mainly  
389 below 10 W m<sup>-2</sup> during contrasting weather conditions. Due to the spatial separation of 156 m between  
390 our sensors and the reference solar radiation measurements and the differences in response speed, we  
391 rejected the cloud passage time intervals. The 645 and 705 nm wavebands seems to correct effects of  
392 cloud have on the GHI where irradiance is enhanced below 500 nm and reduced due to water absorption  
393 bands at wavebands > 1 μm.

394 The remaining uncertainty of the clear day calibration is mainly related to small levelling uncertainties or  
395 tolerances in input optics of both reference and our sensors. This is visible as a shift from a negative to a  
396 positive bias around 12 UTC (Figure 13).



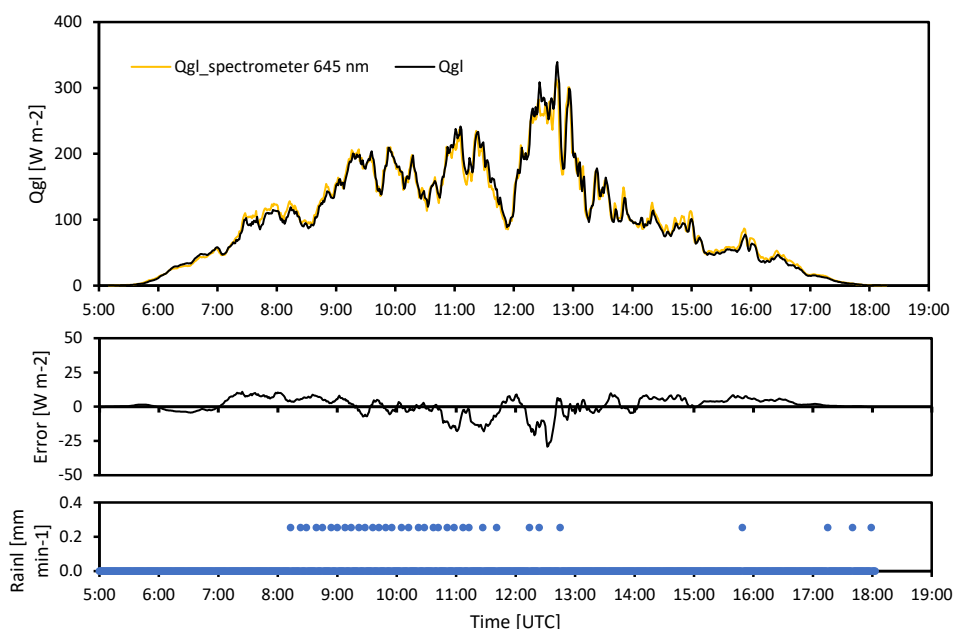
397

398 Figure 13: Comparison between GHI ( $Q_{gl}$ ) measured using a pyr heliometer (converted to horizontal  
399 component) + diffuse radiation and a calibrated FROST with 2 mm diffuser and 1 correction filter,  
400 Veenkampen weather station, 19 March 2022.



401

402 Figure 14: Cloudy weather conditions in the morning, some clearing in the afternoon, 1 minute averaged  
403 data, error plot 10 min running mean, Veenkampen weather station, 14 March 2022.



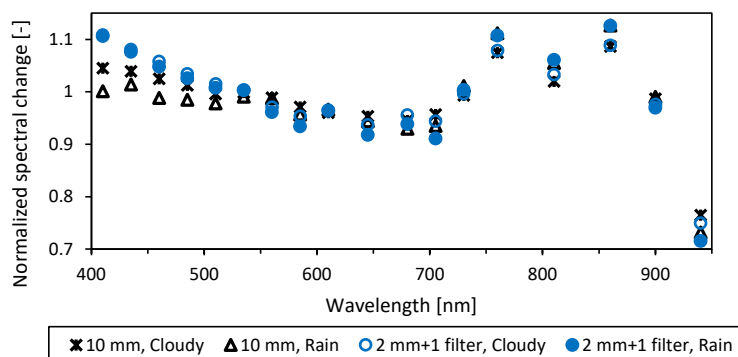
404

405 Figure 15: Rainy day, no removal of water from the instruments, Error plot: 10 min center weighted  
406 running mean, 1 minute data, Veenkampen weather station, 31 March 2022.

407 The instruments were not dried during the precipitation event (Figure 16).

408 The two instruments, one with a 10 mm diffuser and the second version with a 2 mm diffuser and  
409 crosstalk correction filter on the blue sensor were used to calculate the spectral change due to cloudy or  
410 rainy weather conditions. Data from the Figures 13-15 experiments were used and, of the three  
411 contrasting days, the 11-12 UTC intervals were averaged and normalized for the average spectral signal  
412 of the 18 wavebands. Figure 16 shows that the 940 nm waveband is very sensitive to moisture with a  
413 reduction of more than 20% as compared to its nearest waveband. Accordingly, it can be used to derive  
414 information about atmospheric moisture such as column water vapor. Both cloudy and rainy conditions  
415 modify the spectra in a similar way. The low enhancement in the first four wavebands of the instrument  
416 with the 10 mm diffuser version is related to the strong crosstalk in the near infrared. The corrected  
417 version with the 2 mm diffuser, which contains the crosstalk correction filter, shows an enhancement due  
418 to clouds and in line with the findings by Durand et al., 2021, who had an enhancement below 465 nm.  
419 The 645 or 705 nm as shown in Figures 13-15 seem to have the right amount of sensitivity reduction  
420 due to clouds and rain (slightly stronger) to be used for GHI measurements. It is, however,  
421 recommended to use all 18 bands and use a proper weighting function that reduces sensitivity in the  
422 visible region. We currently have no explanation for the enhancements between 750 and 860 nm.

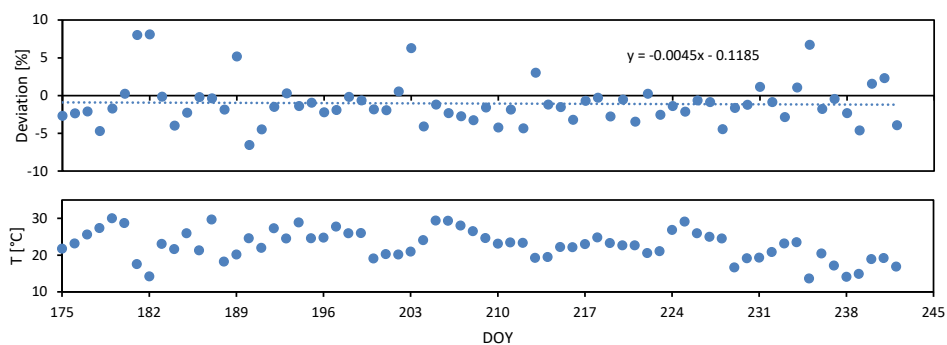




423

424 Figure 16: Two FROST instruments, one with a 10 mm diffuser and one with a 2 mm diffuser and  
425 correction filter. Normalized spectral change of cloudy (14 March, 2022) and rainy weather (31 March,  
426 2022) compared to a cloud free day (19 March 2022), Veenkampen weather station, data averaged  
427 between 11 and 12 UTC for each day.

428 The long-term drift was tested at the Lindenberg rooftop observatory. One instrument was measuring  
429 from 22 June till 31 August 2021 (without any 0.1 s measurement missing). These 2.5 months of data  
430 were converted to GHI values by using only one relatively clear day (13<sup>th</sup> August) and compared with  
431 their reference pyranometer. The values between 12 and 13 h UTC were averaged and the values were  
432 increased by 2% at temperatures below 21°C to correct for the diffuser temperature dependent  
433 transmission according to Figure 12. The diffuser correction practically removed all long-term drift  
434 (Figure 17).



435

436 Figure 17: Long-term stability of FROST, during a 2.5 month comparison experiment at Lindenberg.  
437 Measurements corrected for diffuser transmission change at 21°C.

438

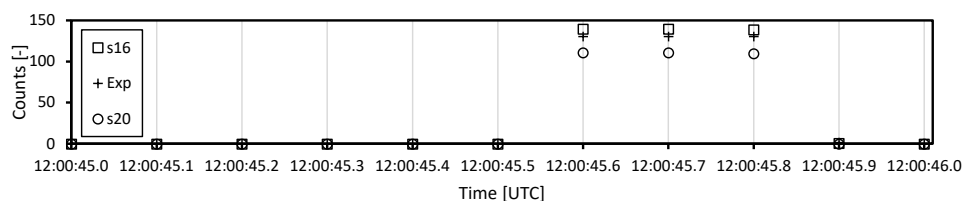
### 439 3.4 Spatial measurements and synchronization

440 For spatial measurements, exact synchronization is essential. Our GNSS solution uses the hardware  
441 timing pulse of the GNSS to trigger a measurement. To illustrate the synchronization performance we  
442 set-up 3 stand-alone FROST sensors and let them run for 1 hr outdoors. We then placed them in a dark  
443 room and at 12:00:45.6 UTC a LED light source was switched on for 0.3 s. Figure 18 shows 1.1 s of  
444 collected 10 Hz data of the 610 nm waveband. The response appears instantaneous and perfectly  
445 synchronized. There is still an integration time for each measurement and this was set at 14 ms for  
446 FROST s16 and s20 and, for testing purposes, twice as long for the experimental version with a less



447 transparent diffuser to get more signal. This instrument is denoted with “Exp” in Figure 18. Therefore,  
 448 the “Exp” FROST occasionally showed a small delay and illustrates the importance of configuring all  
 449 sensors with the same integration time. Figure 18 also shows that the instruments have no zero offset  
 450 errors.

451



452

453 Figure 18: Example of synchronization, response speed and zero offsets of three standalone instruments  
 454 (uncalibrated). All three use their own GNSS for synchronization. Light pulse of 0.3 s generated by a LED  
 455 lamp.

456 The full sensor readout requires 2 integration cycles with each cycle measuring 12 channels (see Table  
 457 3). As a result, there is a maximum of one integration cycle delay between certain channels (with our  
 458 default settings: maximum 28 ms). Six channels are measured twice within one default measurement  
 459 cycle (Table 3). For critical synchronization applications, it is possible to measure only 12 of the 18  
 460 channels during each measurement cycle.

461 Table 3: Readout order during one full measurement cycle.

R	S	T	U	V	W	G	H	I	J	K	L	A	B	C	D	E	F
610nm	680nm	730nm	760nm	810nm	860nm	560nm	585nm	645nm	705nm	900nm	940nm	410nm	435nm	460nm	485nm	510nm	535nm
	1	1	1	1	1	1	1	1	1	1	1	1	1	1	1	1	1
	2	2	2	2	2	2	2	2	2	2	2	2	2	2	2	2	2

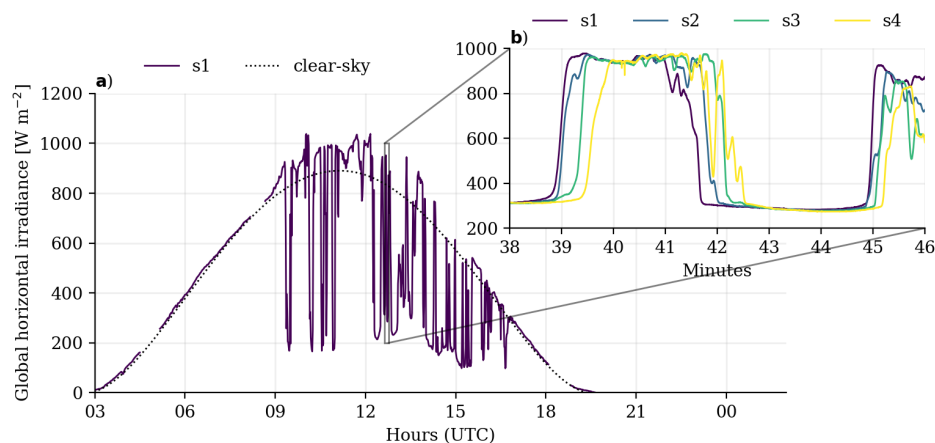
462

463 The downside of a fast integration cycle is a smaller output signal. The 10.6 mm diffuser reduces the  
 464 light onto the detector significantly, approximately 120 to 30 counts per channel at  $650 \text{ W m}^{-2}$ . The 2  
 465 mm diffuser increases the signal by a factor of 4. Longer integration times are considered but should be  
 466 less than 50 ms to assure a sustained 10 Hz output (two integration cycles < 100 ms). Additional time is  
 467 needed for data communication. The AMS spectroscopy sensor output is in ASCII format and therefore  
 468 more digits require more time to transmit.

469 For the measurement campaign in Falkenberg, Germany, a large 2D sensor grid was deployed with a 50  
 470 m grid spacing. It is a good illustration of the spatial dynamics of GHI during partly-cloudy conditions.  
 471 The 1 min averaged data at one point shows the cloud enhancements and the 10 Hz measurements show



472 the high dynamics and spatial variation along a 150 m transect (Figure 19).



473

474 Figure 19: 10 Hz measurements of spatial variation of GHI at four locations along a 150 m west-east  
 475 transect (b) compared to one location (a) at 1 minute averages. The dashed line shows the CAMS  
 476 McClear clear-sky product. Falkenberg, Germany, 27 June, 2021.

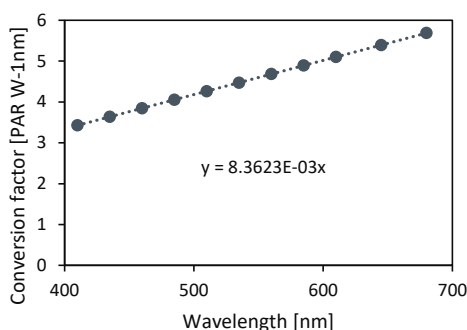
### 477 3.5 Photosynthetic Active Radiation

478 Sensors for measuring Photosynthetic Active Radiation (PAR) are usually constructed using a silicon  
 479 photo diode and a light bandpass filter from 400 to 700 nm. Photosynthesis is a quantum process and  
 480 therefore measurement are usually expressed as a Photosynthetic Photon Flux Density (PPFD,  $\mu\text{mol}$   
 481  $\text{photons m}^{-2} \text{s}^{-1}$ ). The sensor therefore must account for the larger number of photons at larger  
 482 wavelengths (per  $\text{W m}^{-2} \text{nm}^{-1}$ ). The wavelength sensitivity is such that the sensitivity at 700 nm  
 483 wavelength is 1.75 times larger than at 400 nm. In our case, we have 11 well-defined wavebands within  
 484 the PAR region. Therefore, a digital filter can be used to calculate PPFD. Since the sensor outputs in  $\text{W m}^{-2}$   
 485  $\text{nm}^{-1}$ , it must be converted to PPFD by calculating the number of moles per joule per waveband.

486 The photon energy ( $E_n$ ) at each waveband ( $n$ ) is related to wavelength by the speed of light ( $c$ ) and the  
 487 Planck constant ( $h$ ):  $E_n = \frac{hc}{\lambda_n}$ . The photons ( $P$ ) per  $\text{m}^2$  are:  $P_n = \frac{R_n}{E_n}$ , where  $R_n$  is the irradiance measured at  
 488 each waveband. The number of moles is linked to the number of photons through Avogadro's number ( $A$ )  
 489 and integration over all 11 wavebands yields the PPFD:

$$490 \text{PPFD} = (700 - 400) \int_{n=1}^{11} P_n / A n_{max} \quad (1)$$

491



492

493 Figure 20: Conversion factor for each waveband to calculate PPFD [ $\mu\text{mol}$ ].

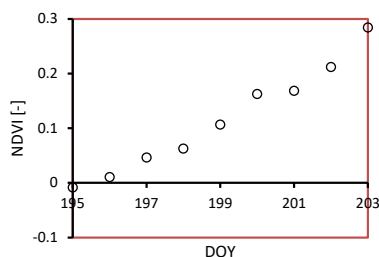
494 The correction per waveband is depicted in Figure 20. The PPFD in Figure 10, lower panel, and the  
495 spectra calculated from the 2 mm diffuser version with two correction filters according to Eq. 1 is  $1293$   
496  $\mu\text{mol m}^2 \text{s}^{-1}$ .

497 Note that the filter characteristics can be adapted for a vegetation specific photosynthesis spectral  
498 response.

### 499 3.6 Vegetation development

500 The FROST was tested during a field experiment in La Cendroza, Spain (Lat: 41.692537, Long:  
501 0.931540) (Liaise Campaign, Boone et al., 2021) from 14-22 July 2021. The instrument was placed on  
502 the bare soil surface at the moment the Alfalfa vegetation started to develop. The Normalized Difference  
503 Vegetation Index (NDVI) index  $(\text{NIR}-\text{VIS})/(\text{NIR}+\text{VIS})$  is used in remote sensing to quantify crop growth;  
504 a low value is bare soil and a value of 1 represents a full-grown crop. It can be computed from at least  
505 two wave bands, one in the near infrared ( $>700 \text{ nm}$ ) and a second waveband in the visible range. The  
506 two wave bands 680 and 730 nm in version 1 that are not affected by infrared crosstalk and both  
507 measure at the same sensor chip were selected to assure that both channels would have the same  
508 viewing angle. Figure 21 shows daily values of NDVI.

509



510



511

512

513



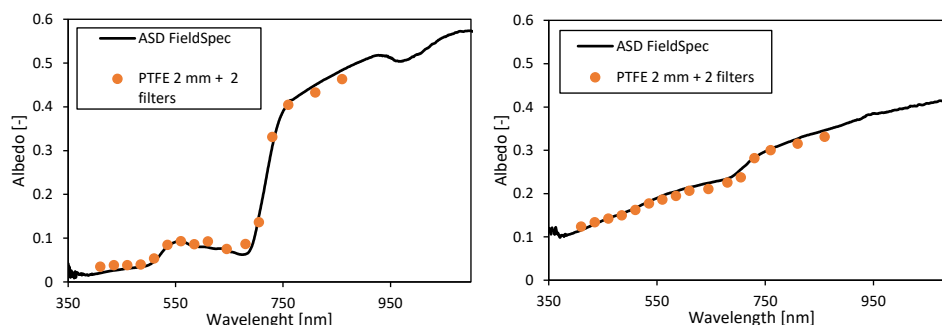
514 Figure 21: NDVI measurements calculated from FROST (with 10 mm diffuser) 680 and 730 nm  
515 wavebands located inside an alfalfa canopy. Bottom left: Sensor (top at about 8 cm height) placed on the



516 surface in between alfalfa, crop height 30 cm, (18 July); Top right: alfalfa crop on 14 July (crop height 23  
517 cm); Bottom right: alfalfa crop (height 48 cm) on 22 July; Spain from 14-22 July 2022.

### 518 3.7 Surface albedo

519 A good test for the quality of the spectral measurements without having to deal with absolute calibration  
520 uncertainties are surface reflectance measurements. The typical spectral reflectance signature of a  
521 healthy vegetation has two minima in the visible range at 500 and 675 nm and a small peak at 550 nm.  
522 Beyond 750 nm it is strongly reflective (about 50%). A bare soil surface, in this case a sandy soil patch  
523 from a very deep soil layer that surfaced during the recent drilling of a well at our weather station,  
524 served as a bare soil plot and had a negligible organic soil fraction. The ASD FieldSpec was equipped with  
525 a cosine collector and operated in irradiance mode. Weather conditions were sunny with low soil moisture  
526 content of the bare soil. The comparison is good considering the difficulty of sampling the same spot for  
527 both instruments due to differences in cosine response, size of sensor head and levelling (Figure 14).



528

529 Figure 22: Spectral reflectance as measured by the FROST and the ASD FieldSpec with cosine collector.  
530 Left panel: Spectral reflectance of grassland, Veenkampen weather station, 14:12 UCT 15 May 2022,  
531 Right panel: Sandy soil (dry, no organic fraction), 14:06 UTC 15 May 2022.

532 The small underestimation of the 810 and 860 nm channels is related to the small cross correlation with  
533 smaller wavelengths (Figure 22).

### 534 4. Discussion

535 Tran and Fukazawa, 2020, used the same AMS spectroscopy sensor to determine optical properties of  
536 fruit, but they did not use LEDs as light sources as recommended by the manufacturer. Their halogen  
537 light source emits much infrared light >1000 nm and therefore all their blue sensor and 2 of their 6 red  
538 sensor channels were greatly affected by infrared crosstalk. This is something they may not have been  
539 aware of because the AMS spectroscopy sensor datasheet does not show the filter response above 1000  
540 nm. Their instrument performance would improve using our proposed correction filters.

541 To date, we have not used the instrument at large zenith angles. Although the proposed cosine  
542 correction appears to give good results, we will continue to further improve the cosine collector for large  
543 zenith angles.

### 544 5. Concluding remarks

545 The FROST instrument will enable new research opportunities. It is much faster than traditional  
546 thermopile pyranometers and the low cost enables the deployment of large sensor grids. It can be  
547 deployed very quickly because it is a fully stand-alone, "plug and play" solution and measurements are  
548 always fully synchronized to UTC within at least a  $\mu$ s. The instrument has superior linearity (<0.2%), the  
549 temperature coefficient is very low (-250 ppm K<sup>-1</sup>), and consistent among three tested instruments. In  
550 contrast to thermopile sensors, the FROST has no zero-offset errors. The drift with time appeared



551 insignificant during a two and a half month field test. Compared to PAR sensors, FROST can resolve the  
552 PAR spectra in 11 narrow wavebands (FWHM: 20 nm). This makes it possible to study wavelength  
553 dependent photosynthesis responses of, for example, chlorophyll A and B. This is also relevant in canopy  
554 profile studies where solar irradiance extinction through a canopy modifies its light spectra. The fast  
555 response makes it possible to investigate the impact of the growth and wind induced movements of  
556 vegetation on radiation fluctuations.

#### 557 **Author contributions**

558 B.H. wrote the manuscript draft, methodology of synchronization, fast spatial spectral irradiance  
559 measurements, instrument software, electronics and mechanical design, investigation and visualization  
560 of spectral response, thermal sensitivity; W.M. organized the Germany and Spain field campaigns  
561 including data organization and visualization of 2D performance in Figure 19; W.M. and B.H. did the  
562 cosine collector and long-term stability experiments and analysis; C.v.H. is the PI of the Shedding Light  
563 On Cloud Shadows (SLOCS) project to which this research belongs and has designed the research  
564 programme that depends on this instrument; W.M. and C.v.H. reviewed and edited the manuscript.

#### 565 **Acknowledgements**

566 We are grateful for the support and use of the optical calibration facility of DWD Lindenberg and many  
567 thanks go to Stefan Wacker and Steffen Gross. We also thank Harm Bartholomeus (Wageningen  
568 University, Remote sensing group) for providing the ASD FieldSpec and Emilie Wientjes (Wageningen  
569 University) for assistance with their Cary spectrophotometer.

570 C.v.H., W.M., and B.H. acknowledge funding from the Dutch Research Council (NWO) (grant:  
571 VI.Vidi.192.068).

572

#### 573 **References**

574 Boone, A., Bellvert, J., Best, M., Brooke, J., Canut-Rocafort, G., Cuxart, J., Hartogensis, O., e Moigne, P.,  
575 Miró, J. R., Polcher, J., Price, J., Quintana Seguí, P., & Wooster, M.: Updates on the International Land  
576 Surface Interactions with the Atmosphere over the Iberian Semi-Arid Environment (LIAISE) Field  
577 Campaign. *GEWEX News*, 31(4), 17–21, 2021.

578 Cahalan, R.F., Oreopoulos, L., Marshak, A., Evans, K.F., Davis, A.B., Pincus, R., Yetzer, K.H., Mayer, B.,  
579 Davies, R., Ackerman, T.P., Barker, H.W., Clothiaux, E.E., Ellingson, R.G., Garay, M.J., Kassianov, E.,  
580 Kinne, S., Macke, A., O'hirok, W., Partain, P.T., Prigarin, S.M., Rublev, A.N., Stephens, G.L., Szczap, F.,  
581 Takara, E.E., Wen, T.V.G., Zhuravleva, T.B.: THE I3RC: Bringing Together the Most Advanced Radiative  
582 Transfer Tools for Cloudy Atmospheres, *Bull. Am. Meteorol. Soc.*, 86-9, 1275-1293,  
583 <https://doi.org/10.1175/BAMS-86-9-1275>, 2005.

584 Durand, M., Murchie, E.H., Lindfors, A.V., Urban, O., Aphalo, P.J., Robson, M.: Diffuse solar radiation and  
585 canopy photosynthesis in a changing environment. *Agricultural and Forest Met.*, 311, Article 108684,  
586 <https://doi.org/10.1016/j.agrformet.2021.108684>, 2021.

587 Guichard, F. and Couvreur, F.: A short review of numerical cloud-resolving models. *Tellus A: Dynamic  
588 Meteorology and Oceanography*, 69:1, 1373578, <https://doi.org/10.1080/16000870.2017.1373578>,  
589 2017.

590 Kreuwel, F. P. M. , Knap, W. H., Visser, L. R., Sark, W. G. J. H. M. van, Vilà-Guerau de Arellano, J.,  
591 Heerwaarden, C. C. van: Analysis of high frequency photovoltaic solar energy fluctuations. *Solar Energy*  
592 206: 381-389, <https://doi.org/10.1016/j.solener.2020.05.093>, 2020

593 Lohmann, G. M.: Irradiance variability quantification and small-scale averaging in space and time: a  
594 short review. *Atmosphere* 9 (7): 264. <https://doi.org/10.3390/atmos9070264>, 2018.



- 595 Lopes Peirera, R., Trindade, J., Goncalves, F., Suresh, L., Barbosa, D., Vazao, T.: A wireless sensor  
596 network for monitoring volcano-seismic signals. *Nat. Hazards Earth Syst. Sci.*, 14: 3123-3142,  
597 <https://doi.org/10.5194/nhess-14-3123-2014>, 2014
- 598 Nann, S. and Riordan C.: Solar spectral irradiance under clear and cloudy skies: measurements and a  
599 semiempirical model, *J. Appl. Meteor.*, 21:447-462, <https://doi.org/10.1175/1520->  
600 [0450\(1991\)030<0447:SSIUCA>2.0.CO;2](https://doi.org/10.1175/1520-0450(1991)030<0447:SSIUCA>2.0.CO;2), 1991.
- 601 Tran, N.T., and Fukuzawa, M.: A portable spectrometric system for quantitative prediction of the soluble  
602 solids content of apples with a pre-calibrated multispectral sensor chipset. *Sensors*, 20: 5883,  
603 <https://doi.org/10.3390/s20205883>, 2020.
- 604 Veerman, M.A., Pedruzo-Bagazgoitia, X., Jakub, F., Vilà-Guerau de Arellano, J., Heerwaarden, C.C. van,  
605 2020: Three-dimensional radiative effects by shallow cumulus clouds on dynamic heterogeneities over a  
606 vegetated surface. *Journal of Advances in Modeling Earth Systems*, 12,  
607 <https://doi.org/10.1029/2019MS001990>, 2020.
- 608 Yliantilla, L. and Schreder, S., 2004: Temperature effects of PTFE diffusers. *Optical Materials*, 27, 1811-  
609 1814, <https://doi.org/10.1016/j.optmat.2004.11.008>, 2004.
- 610 Yordanov, G.H., Saetre, O., Midtgard, O.: 100-millisecond resolution for accurate overirradiance  
611 measurements. *IEEE Journal of Photovoltaics*, 3, 1354-1360,  
612 <https://doi.org/10.1109/JPHOTOV.2013.2264621>, 2013.
- 613 Yordanov, G.H.:A study of extreme overirradiance events for solar energy applications using NASA's  
614 13RC Monte Carlo radiative transfer model. *Solar Energy*, 122, 954-965,  
615 <https://doi.org/10.1016/j.solener.2015.10.014>, 2015.
- 616
- 617